Modeling two-phase flow in three-dimensional complex flow-fields of proton exchange membrane fuel cells

CrossMark

Jinyong Kim, Gang Luo, Chao-Yang Wang*

Electrochemical Engine Center (ECEC), Department of Mechanical & Nuclear Engineering, The Pennsylvania State University, University Park, PA 16802, USA

HIGHLIGHTS

- Forchheimer's inertial effect is dominant in PEMFCs with 3D complex flow-fields.
- Forchheimer's inertial effect enhances liquid water removal and mass transport.
- PEMFCs with 3D complex flow-fields are robust and efficient at high current density.

ARTICLE INFO

ABSTRACT

3D fine-mesh flow-fields recently developed by Toyota Mirai improved water management and mass transport in proton exchange membrane (PEM) fuel cell stacks, suggesting their potential value for robust and high-power PEM fuel cell stack performance. In such complex flow-fields, Forchheimer's inertial effect is dominant at high current density. In this work, a two-phase flow model of 3D complex flow-fields of PEMFCs is developed by accounting for Forchheimer's inertial effect, for the first time, to elucidate the underlying mechanism of liquid water behavior and mass transport inside 3D complex flow-fields and their adjacent gas diffusion layers (GDL). It is found that Forchheimer's inertial effect enhances liquid water removal from flow-fields and adds additional flow resistance around baffles, which improves interfacial liquid water and mass transport. As a result, substantial improvements in high current density cell performance and operational stability are expected in PEMFCs with 3D complex flow-fields, compared to PEMFCs with conventional flow-fields. Higher current density operation required to further reduce PEMFC stack cost per kW in the future will necessitate optimizing complex flow-field designs using the present model, in order to efficiently remove a large amount of product water and hence minimize the mass transport voltage loss.

© 2017 Elsevier B.V. All rights reserved.

1. Introduction

Proton exchange membrane fuel cells (PEMFCs) are regarded as one of the most promising alternative power sources for automotive applications due to their low pollutant emission, low operating temperature and high-power density. The central issue that still prevents PEM fuel cell vehicles (FCVs) from mainstream commercialization is high cost of fuel cell stacks owing to use of the noble metal platinum (Pt) as a catalyst. One solution is to increase cell operating current density, in order to enhance power density of fuel cell stacks and to decrease fuel cell stack size and material usage. Under high current density operation, however, PEM fuel cells are susceptible to water flooding and oxygen starvation due to huge rate of electrochemical reactions, which may cause detrimental loss of stability and performance [1]. Therefore, proper management of liquid water and mass transport are of primary importance to development of next generation FCVs with high power and compact fuel cell stacks.

Recently, three-dimensional (3D) complex flow-field designs have attracted much attention due to capability of significantly enhancing liquid water management and oxygen transport. Fig. 1a schematically shows 3D complex flow-field structure of a recently commercialized vehicle, Toyota Mirai [2]. Unlike conventional flow-fields, 3D complex flow-fields feature repeating 3D micro-lattices, which act as baffles and induce frequent micro-scale interfacial flux between GDL and flow-fields. Due to this repeating micro-scale convective flow, oxygen transport to catalyst layer (CL) and liquid

* Corresponding author.
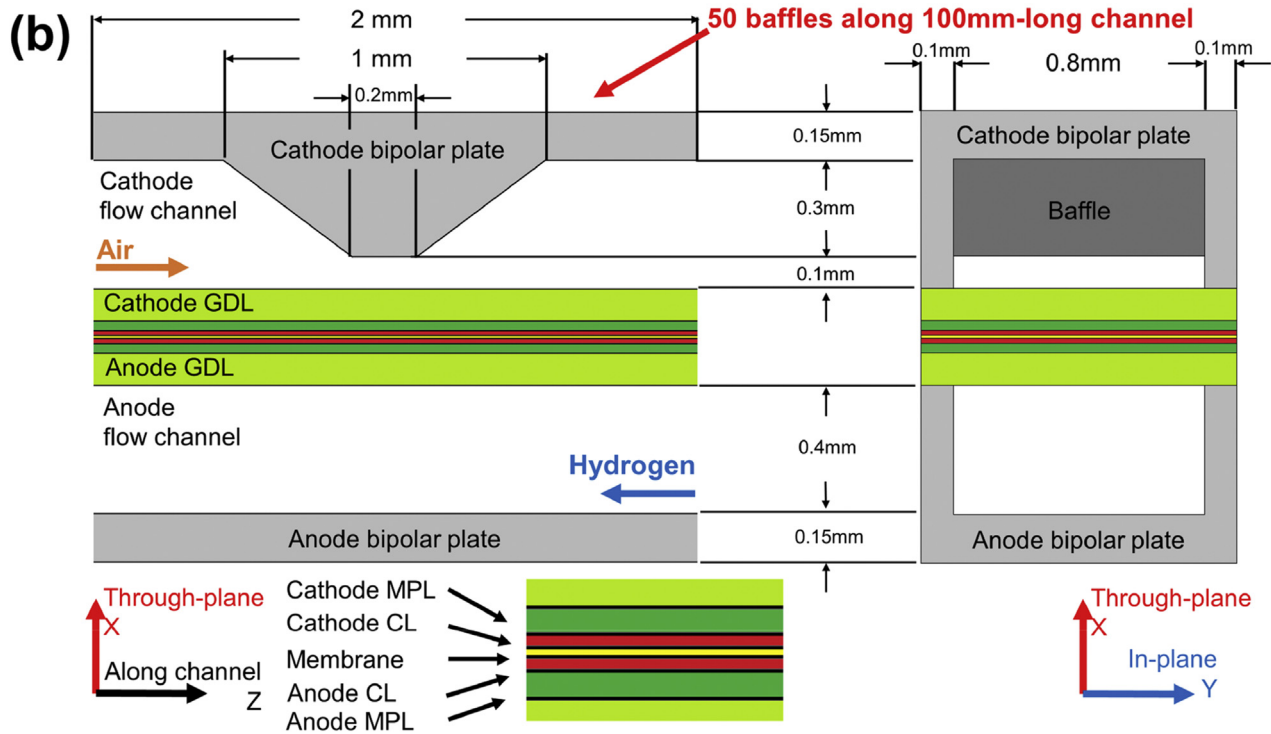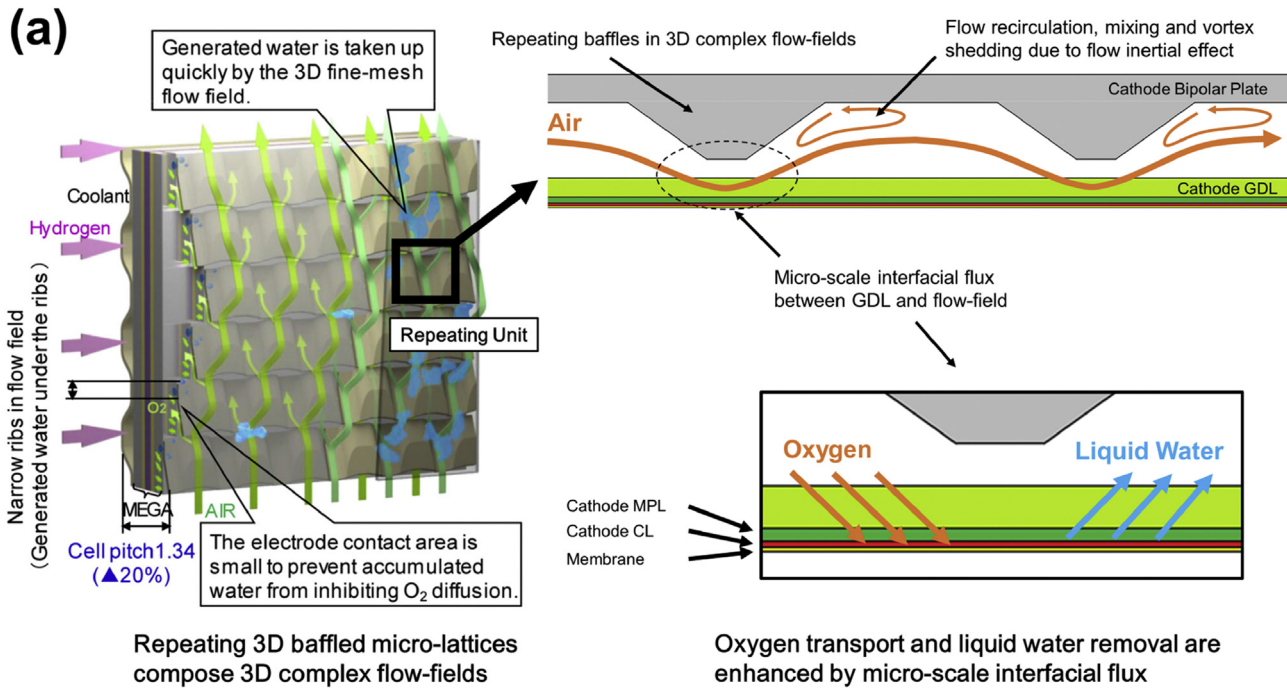   E-mail address: cxw31@psu.edu (C.-Y. Wang).

Fig. 1. (a) Schematics of PEM fuel cell with 3D complex flow-field (Toyota Mirai flow-field [2] is taken as an example) (b) Computational geometry.

water removal from GDL are significantly enhanced. By using innovative 3D fine mesh flow-field, along with the improvements of MEA material, Toyota Mirai achieved significant increase of cell performance (up to 2.4 times increase of limiting current density compared to their 2008 model fuel cell stack design) as well as power stability [2–4]. In addition to the Mirai example, several recent experimental studies have shown cell performance increase

of up to 5–30% by using baffled flow-fields. Heidary et al. [5] conducted experimental studies and reported the increase of cell performance by up to 30% with different configurations of partial or full blockages in flow channels. Thitakamo et al. [6] experimentally showed 20–30% performance increase from cell with mid-baffle interdigitated flow-field compared to cell with conventional flow-field. Han et al. [7] studied the effect of repeated wavy-shape

baffles in flow channels both experimentally and numerically and showed 6% increased performance compared to regular flow channel.

Numerous examples shown above indicate the great potential of 3D complex flow-fields toward further innovations in PEMFC technology. However, two-phase fuel cell modeling of such flow-fields has been absent. Regarding this topic, several single-phase [7–12] and two-phase flow calculations under mist-flow assumptions [13,14] have been performed to date, which result in unrealistic estimation of two-phase flow behavior in flow channel due to over-simplified treatment of two-phase flow. Considering the significances of two-phase behavior in PEMFCs and potentials of 3D complex flow-field designs on cell performance, modeling two-phase behavior in 3D complex flow-fields is of urgent interest, especially for cell-scale simulations to accelerate mainstream commercialization of PEMFCs.

Unlike conventional PEMFC flow-fields, complex flow structure such as flow expansion/contraction, recirculation and vortex shedding, which are all categorized into flow inertial effects, are expected to be dominant in 3D complex PEMFC flow-fields due to repeating baffles [8,9,11,12,14]. In this case, the flow inside 3D complex flow-fields no longer follows Darcy's law and additional inertial effect, i.e. the Forchheimer's effect, plays important roles. Previous macroscopic modeling approaches, such as the multi-phase mixture (M^2) model [15–19], are based on two-phase Darcy's law and the Forchheimer's inertial effect have not been considered due to simple fully-developed flow structure and low current density operation (~1 A cm^{-2}) in conventional PEMFCs. Since next generation PEMFCs with 3D complex flow-fields are expected to operate at much higher current densities, Forchheimer's effect is crucial and should be considered in two-phase flow modeling.

In this work, we propose, for the first time, a two-phase fuel cell model based on two-phase Forchheimer extension to describe macroscopic liquid water and mass behavior in 3D complex flow-fields, especially under high current density operation. We explore role of Forchheimer's inertial effect on liquid water and mass transport behavior inside flow channel and gas diffusion layer (GDL) of PEMFCs with 3D complex flow-fields, by comparing present model with the conventional M^2 model. Furthermore, we discuss the differences between PEMFCs with 3D complex flow-fields and regular straight channels in terms of cell performance and operational stability.

2. Numerical model

The similarities between flow in porous media and micro-channel has been recognized in a number of prior studies [16–30]. Numerous attempts have been made to model the single and two-phase flow in micro-channel with Darcy's law by looking at micro-channels as porous media for applications in heat-exchangers [21–27] and PEMFC [16–19,28–30] simulations. On the other hand, well-known models of flow in porous media, such as Kozeny-Carman equation [31,32] and Ergun equation [33], are based on Kozeny assumption [31] that structure of porous media is similar to a collection of micro-channels. Based on the similarity, Wang et al. [19] developed two-phase flow model based on two-phase Darcy's law for conventional flow-fields of PEMFCs, such as straight channels, by considering the flow-field of PEMFCs as structured and ordered porous media.

As seen in Fig. 1a, the geometries of 3D complex flow-fields strongly resemble random porous medium, rather than structured and ordered porous medium. To study the fundamental flow physics involved in 3D complex flow-fields, we first estimate the range of pore Reynolds number inside 3D complex flow-fields, which is defined as

$$\text{Re}_p = \frac{UL_p}{\nu_p} \tag{1}$$

where U is the characteristic velocity scale, L_p is the characteristic pore size and ν_p is the kinematic viscosity of fluid inside porous medium. The typical range of pore Reynolds number of flow channels of PEMFCs at high current density (2~4 A cm^{-2}) falls on the magnitude of 100, by using typical operation parameters of $U = 5–10$ m s^{-1}, $L_p = 0.1–1$ mm and $\nu_p = 2.0 \times 10^{-5}$ m^2 s^{-1}. As prior studies [34–39] reported that inertial effect is no longer negligible and becomes as important as the viscous effect when $\text{Re}_p > 100$ in random porous media, inertial pressure loss described by Forchheimer's inertial term should be considered in two-phase model. In the following sections, we attempt to incorporate the Forchheimer's inertial term into the well-known M^2 formulation.

2.1. Permeability and Forchheimer's inertial flow coefficient of 3D complex flow-fields

Momentum equation in homogeneous-isotropic porous media under Forchheimer's inertial regime can be described by Darcy-Forchheimer's law as

$$-\nabla P = \frac{\mu}{K} \overrightarrow{u} + \beta \rho |\overrightarrow{u}| \overrightarrow{u} \tag{2}$$

where K and β are permeability and non-Darcy flow coefficient (also known as Forchheimer's coefficient), respectively. Numerous studies have been conducted to estimate the range of permeability and Forchheimer's inertial flow coefficient based on porosity and pore diameter. The most well-known relations are Kozeny-Carman equation [31,32] for permeability estimation and Ergun's equation [33] for Forchheimer's inertial flow coefficient estimation.

The original form of Ergun's equation can be written as

$$-\nabla P = \frac{32\alpha_{Er}}{\varepsilon D_h^2} \mu \overrightarrow{u} + \frac{\beta_{Er}}{2\varepsilon^2 D_h} \rho |\overrightarrow{u}| \overrightarrow{u} \tag{3}$$

where D_h is effective hydraulic diameter of porous media defined as $4 \times$ total surface area of porous media divided by volume of void region in porous media. The first term and the second term in RHS in Eq. (3). are Darcy's viscous term and Forchheimer's inertial term, respectively. Since each term is modeled based on Kozeny's assumption, effective hydraulic diameter is the key parameter that determines permeability and non-Darcy flow coefficient in Ergun's equation. The empirical correction factor α_{Er} and β_{Er} are introduced to account for the repeated sinusoidal flow contraction and expansion effect, which typically range from 1 to 10 and 1–6, respectively [33].

By looking at the 3D complex flow-fields in PEM fuel cell as a homogeneous and isotropic porous medium with porosity of unity by following the same approach as Wang et al. [19], the Ergun's momentum equation reduces to

$$-\nabla P = \frac{32\alpha_{Er}}{D_h^2} \mu \overrightarrow{u} + \frac{\beta_{Er}}{2D_h} \rho |\overrightarrow{u}| \overrightarrow{u} \tag{4}$$

where Ergun's empirical correction factor α_{Er} and β_{Er} can be obtained from experimental relationships between pressure drop and flow rate. For the CFD simulation, α_{Er} and β_{Er} can be fitted based on relationships between pressure drop and flow rate by simulation of single-phase Navior-Stokes equation. From the Eqs. (2) and (4), it can be found that permeability, K, is equivalent to $D_h^2/(32\alpha_{Er})$ and non-Darcy flow coefficient β, is equivalent to $\beta_{Er}/(2D_h)$.

Table 1
Operating conditions.

Parameters	Value
Anode/cathode inlet pressure	2.0/2.0 atm
Anode/cathode inlet temperature	55/55 °C
Anode/cathode inlet dew point	55/55 °C
Anode/cathode stoichiometry	2.0/2.0
Current density	4.0 A cm^{-2}

Table 2
Physical and geometrical parameters.

Parameters	Value
Anode/Cathode GDL thickness	100 μm
Anode/Cathode MPL thickness	30 μm
Anode/Cathode CL thickness	15 μm
Membrane thickness	10 μm
Contact angle of GDLs/MPLs/CLs/flow-fields	110/120/100/66°
Porosity of GDLs/MPLs/CLs	0.65/0.6/0.5
Permeability of GDLs/MPLs/CLs	$8.0 \times 10^{-12}/5.0 \times 10^{-13}/3.0 \times 10^{-14}$ m^2
Effective hydraulic diameter of conventional/3D complex flow-fields	$5.33 \times 10^{-4}/5.02 \times 10^{-4}$ m
α_{Er} of conventional/3D complex flow-field	0.91/4.35
β_{Er} of conventional/3D complex flow-field	0/1.29
Permeability of conventional/3D complex flow-field	$9.76 \times 10^{-9}/1.81 \times 10^{-9}$ m^2
non-Darcy coefficient of conventional/3D complex flow-field	0/768 m^{-1}
Thermal conductivity of the GDLs/MPLs/CLs	0.5/0.5/1.0 W m^{-1}K^{-1}
Thermal conductivity of the membrane	0.4 W m^{-1}K^{-1}
Thermal conductivity of the bipolar plates	117 W m^{-1}K^{-1}
Equivalent weight of ionomers	0.85 kg mol^{-1}
Density of dry membrane	1800 kg m^{-3}

2.2. Derivation of multiphase mixture model with Forchheimer's inertial effect (M²F model)

Once permeability and Forchheimer's inertial coefficient are

available, momentum equations in porous media for each phase can be expressed by two-phase Darcy-Forchheimer's law as

$$\nabla P_l = -\frac{\mu_l}{KK_{rl}} \overrightarrow{u_l} - \rho_l \beta \beta_{rl} \left| \overrightarrow{u_l} \right| \overrightarrow{u_l} \tag{5}$$

$$\nabla P_g = -\frac{\mu_g}{KK_{rg}} \overrightarrow{u_g} - \rho_g \beta \beta_{rg} \left| \overrightarrow{u_g} \right| \overrightarrow{u_g} \tag{6}$$

where P_k is a pressure field of phase-k, K_{rk} is relative permeability of phase-k and β_{rk} is relative non-Darcy flow coefficient of phase-k. Relative permeability is a ratio of intrinsic permeability of k-phase to absolute permeability and relative permeability typically is a function of water saturation. In this study, relative permeability is described by power law such that $K_{rl} = s^{n_k}$, $K_{rg} = (1-s)^{n_k}$. The exponent constant n_k of 4, 5 are used in flow channel [19] and diffusion media [40], respectively.

Here, we re-define a relative permeability of phase-k as

$$K'_{rk} = K_{rk}\left(1 + \frac{K_{rk}\beta_{rk}K\beta\rho_k \left| \overrightarrow{u_k} \right|}{\mu_k}\right)^{-1} \tag{7}$$

where superscript ′ denotes a non-Darcy parameter. In this study, we consider the case that $K_{rk} = \beta_{rk}^{-1}$ as suggested by prior studies [41–44]. Then, the Eq. (7). reduces to

$$K'_{rk} = K_{rk}(1 + Fo_k)^{-1} \tag{8}$$

where Forchheimer number for phase-k, Fo_k, is defined as $Fo_k = K\beta\rho_k \left| \overrightarrow{u_k} \right| / \mu_k$. The Forchheimer number indicates the influence of flow inertial effect on macroscopic flow behavior [45].

For gaseous phase, the inertial pressure loss is as important as viscous pressure loss in ranges of a pore Reynolds number between 10 and 500 (i.e. $Fo_g \sim 1$) [34–39]. However, the inertial effect of liquid water is negligible compared to inertial effect of gaseous phase (i.e. $Fo_l << Fo_g$) in PEMFC applications due to low mass flow rate of liquid water (less than 10% of total mass flow rate justified by Wang et al. [46]) and high liquid water dynamic viscosity (i.e. $\mu_l \sim 3 \times 10^{-4}$ kg m^{-1} s^{-1}) compared to air dynamic viscosity ($\mu_g \sim 2 \times 10^{-5}$ kg m^{-1} s^{-1}). Therefore, only gas-phase inertial effect
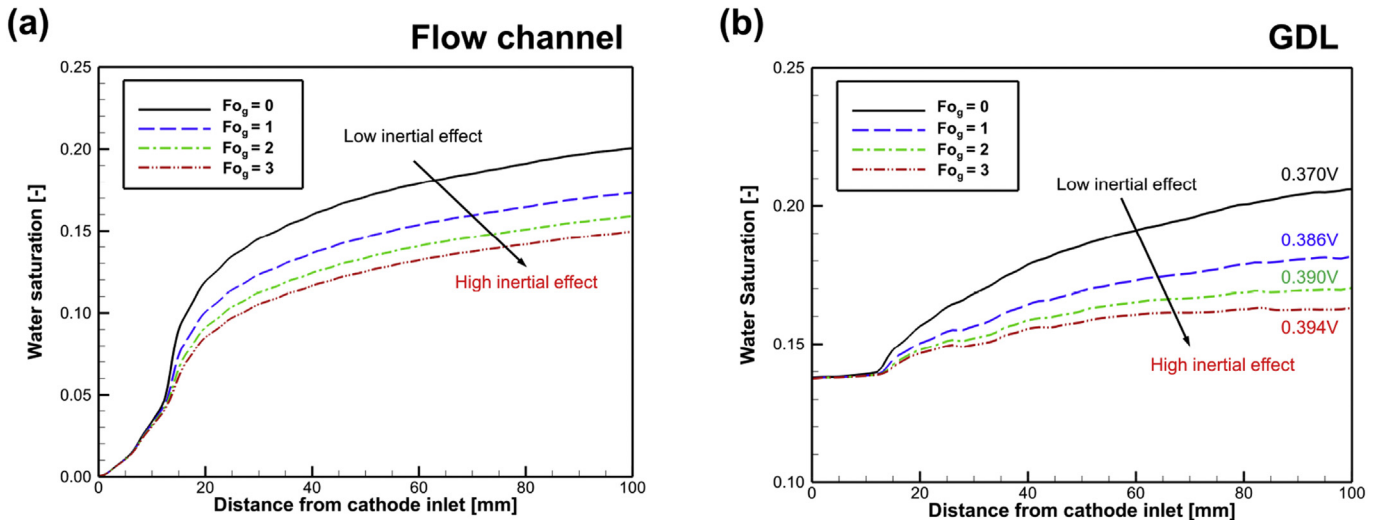
Fig. 2. Cross-sectional averaged water saturation profile of PEMFC with regular flow channel with different gas Forchheimer number ranging from 0 to 3 along channel direction (a) at flow channel (b) at GDL.

is considered in this study.

By using the re-defined relative permeability for gas-phase, Eq. (5) and 6 reduce to

$$\nabla P_l = -\frac{\mu_l}{KK_{rl}} \vec{u_l} \tag{9}$$

$$\nabla P_g = -\frac{\mu_g}{KK'_{rg}} \vec{u_g} \tag{10}$$

The only difference between K'_{rg} and K_{rg} is that one more non-dimensional number is considered to evaluate K'_{rg}, i.e. $K'_{rg} = K'_{rg}(s, Fo_g)$. Therefore, by simply plugging K'_{rg} into K_{rg} and following the same mathematical process in derivation of M^2 model [47–49] starting from Eqs. (9) and (10), the governing equations in the M^2 framework are derived as follows.

Continuity equation:

$$\nabla \bullet (\rho \vec{u}) = 0 \tag{11}$$

Momentum conservation equation:

$$\frac{\rho}{\varepsilon}\left[\frac{\partial \vec{u}}{\partial t} + \frac{1}{\varepsilon}\nabla \bullet (\vec{u}\,\vec{u})\right] = -\nabla P + \nabla \bullet \overrightarrow{\overrightarrow{\tau}} + S'_u \tag{12}$$

Energy conservation equation:

$$\frac{\partial(\rho c_p T)}{\partial t} + \nabla \bullet (\gamma'_T \rho c_p T) = \nabla \bullet \left(k^{eff} \nabla T\right) + S_T \tag{13}$$

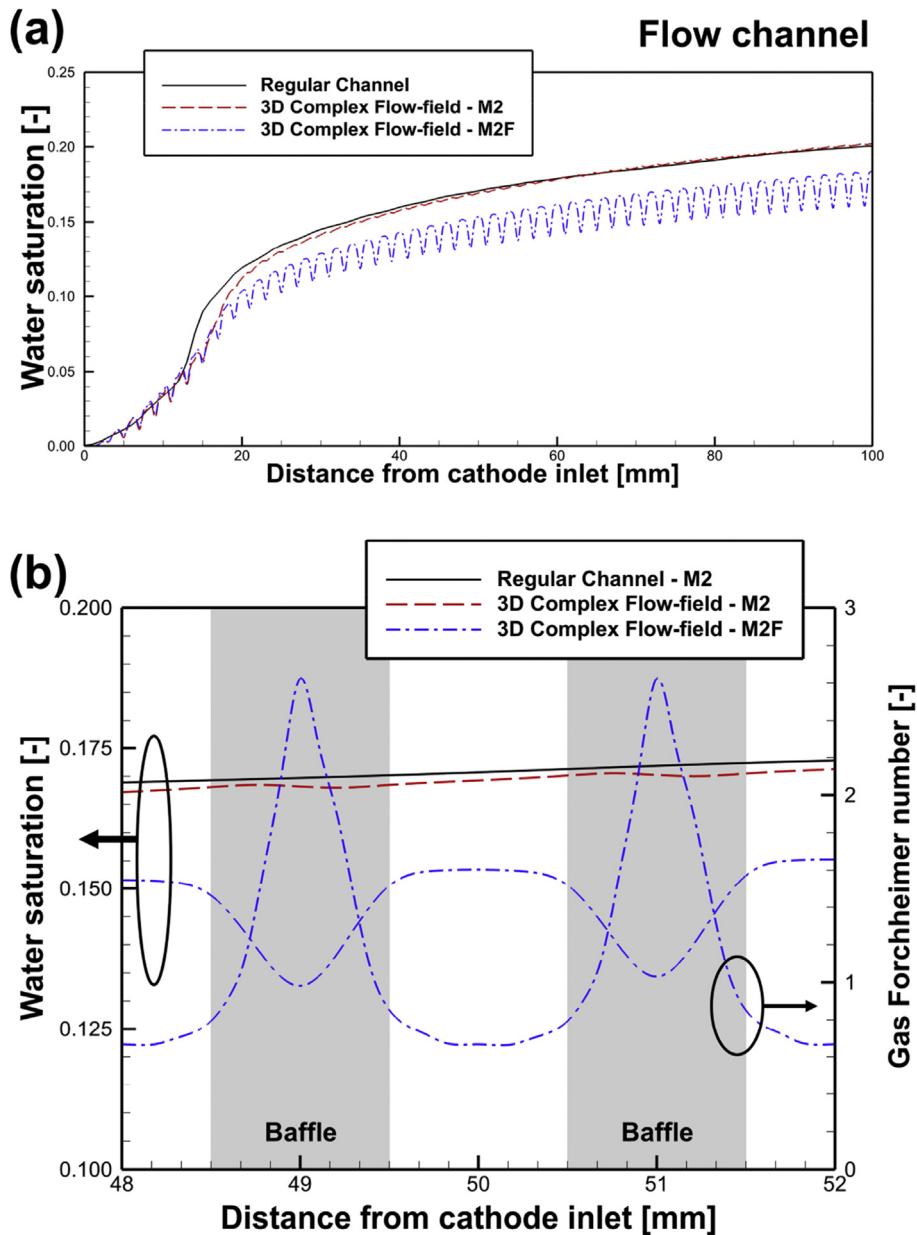Unified species conservation equation of k-species:

Fig. 3. Cross-sectional averaged flow channel water saturation profile along channel direction (a) at whole flow channel (b) at mid-channel region (48 mm < z<52 mm) (gray: baffle region).

$$\varepsilon^{eff}\frac{\partial C^i}{\partial t} + \nabla \bullet \left(\gamma'_c \overrightarrow{u} C^i\right) = \nabla \bullet \left(D_g^{i,eff} \nabla C_g^i\right)$$
$$- \nabla \bullet \left(\left(\frac{mf_l^i}{M^i} - \frac{C_g^i}{\rho_g}\right)\overrightarrow{j}'_l\right) + S_i \tag{14}$$

Charge conservation equation (electrons):

$$0 = \nabla \bullet \left(\sigma^{eff} \nabla \Phi_s\right) + S_{\Phi_s} \tag{15}$$

Charge conservation equation (protons):

$$0 = \nabla \bullet \left(\kappa^{eff} \nabla \Phi_e\right) + S_{\Phi_e} \tag{16}$$

where T, C^k, Φ_s and Φ_e are temperature, species molar concentration, electronic and electrolyte phase potential, respectively. The details of all physical properties, source terms and constitutive relationships in the governing equations are found in Reference [50] and thus are not repeated in this study. The only difference between current modeling and previous M^2 model is that properties with superscript ′ (non-Darcy parameters) are expressed by K'_{rg} instead of K_{rg}. For example, momentum source term S'_u is defined as μ'/K instead of μ/K, where non-Darcy dynamic mixture viscosity μ' is defined as $\mu' = \rho(K_{rl}/\nu_l + K'_{rg}/\nu_g)^{-1}$.

2.3. Simulation cases and numerical methods

The computational geometry is shown in Fig. 1b. A 100 mm-long single straight flow channel is first considered in this study as an example of typical conventional flow-field. For this conventional flow-field, 0.1 million computational cells are used. In order to study the roles of micro-scale interfacial flux and Forchheimer's inertial effect in 3D complex flow-fields, repeating baffles are added to the single straight flow channel and this baffled flow channel is selected as a representative of 3D complex flow-field in this work. Fifty 1 mm-long baffles are equally spaced in the flow channel and 0.7 million computational cells are used to capture complex two-phase behavior.

Operating conditions are listed in Table 1, and physical and geometrical parameters are listed in Table 2. In particular, we consider operating current density of 4 A cm^{-2} [51] in current simulation work to study liquid water and mass transport behavior in next-generation compact fuel cell stack under high power operation. Relative humidity of 100% is used since the effect of dry-wet-dry transition is not within the scope of this study.

All of governing equations are solved with commercial CFD software, Fluent (version 15.0). SIMPLE algorithm [52] is used for pressure-velocity coupling and algebraic multigrid (AMG) method [53] is used for acceleration of computational speed. User defined functions (UDF) are added to customize and update source terms, transport properties and boundary conditions during calculation. In all simulations, water and species imbalance less than 2% are achieved, which are considered as convergence criteria.

3. Results and discussion

### 3.1. Liquid water behavior in flow channel of PEM fuel cell under Forchheimer's inertial effect

Proper management of water inside flow channel is important since water blockage and accumulation in flow channel causes oscillations in cell voltage or even cell shut-down, which are critical to both cell performance and operational stability. We first consider a regular straight channel case in order to explore the

Forchheimer's inertial effect on liquid water behavior when no gas flow penetrations occur between flow channel and GDL, before studying Forchheimer's inertial effect in 3D complex flow-field cases, where strong gas flow penetrations take place between flow channel and GDL due to convective transport by baffles. A series of simulations of PEMFCs with straight flow channel with different prescribed gas Forchheimer numbers ranges from 0 to 3 at 4 A cm^{-2} are carried out and liquid water saturation behavior in flow channel and GDL are compared in Fig. 2. Fig. 2a shows variations of water saturation in flow channel along channel direction. It is evident that the water saturation decreases as inertial effect increases, which implies that the inertial effect improves liquid water removal from flow channel. As a result, better water removal inside GDL is estimated under higher inertial effect according to Fig. 2b, which further increase fuel cell voltage by reducing oxygen diffusion resistance to CL.

In Fig. 3, Forchheimer's inertial effect on liquid water behavior in 3D complex flow-field is studied by comparing M^2 and M^2F model simulation. Fig. 3a plots water saturation distributions of three simulation cases inside flow channel (regular channel case with baseline M^2 model, 3D complex flow-field case with baseline M^2 model and 3D complex flow-field case with proposed M^2F model). According to Fig. 3a, it can be seen that, the water saturation distributions inside 3D complex flow-field and straight channel are similar if Forchheimer's inertial effect is not considered. Unlike M^2 model, however, M^2F model shows not only smaller saturation overall compared to the other two cases, but also sinusoidal behavior. To address the origin of sinusoidal characteristic of water saturation behavior under Forchheimer's inertial effect in detail, water saturation at mid-channel region ($48\ mm < z < 52\ mm$) along with gas Forchheimer number are plotted in Fig. 3b. As Forchheimer's inertial effect becomes more significant in the necking region of flow channel due to increasing gas velocity, liquid water

Table 3
Average water saturation of cathode channel/GDL/MPL and CL.

	Channel	GDL	MPL	CL
Regular channel − M^2	0.144	0.180	0.131	0.189
3D complex flow-field − M^2	0.141	0.154	0.124	0.195
3D complex flow-field − M^2F	0.126	0.132	0.113	0.192
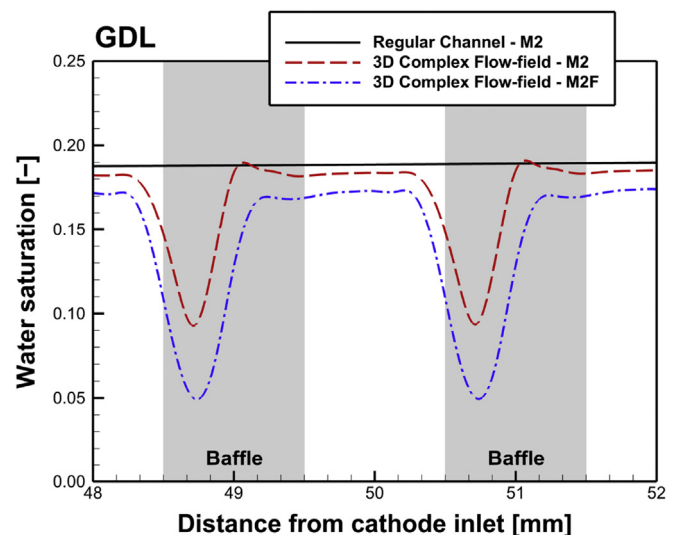
Fig. 4. Cross-sectional averaged GDL water saturation profile along channel direction at mid-channel ($48\ mm < z < 50\ mm$) (gray: baffle region).

under baffle is more effectively removed than non-baffle region. This local variation of Forchheimer's inertial effect causes sinusoidal water saturation behavior in 3D complex flow-field.

3.2. Liquid water behavior in GDL of PEM fuel cell with 3D complex flow-field

Water management inside GDL is of primary importance in terms of both performance and operational stability of PEMFC since water flooding inside GDL causes uneven and poor oxygen transport to catalyst layer that significantly increase mass transport

overpotential [54]. To study the water behavior inside GDL of PEMFCs with 3D complex flow-field at high current density, average water saturations of the three simulation cases at cathode channel/GDL/MPL and CL are first evaluated in Table 3. The differences of water saturation in MPL and CL are not significant among the three cases while considerable amount of water removal inside GDL, roughly 30%, is observed in M^2F simulation of 3D complex flow-field compared to M^2 simulation of regular straight channel. This implies that it is possible to only remove excessive liquid water in GDL while maintaining sufficient membrane hydration using 3D complex flow-field. Table 2 also shows the significance of flow
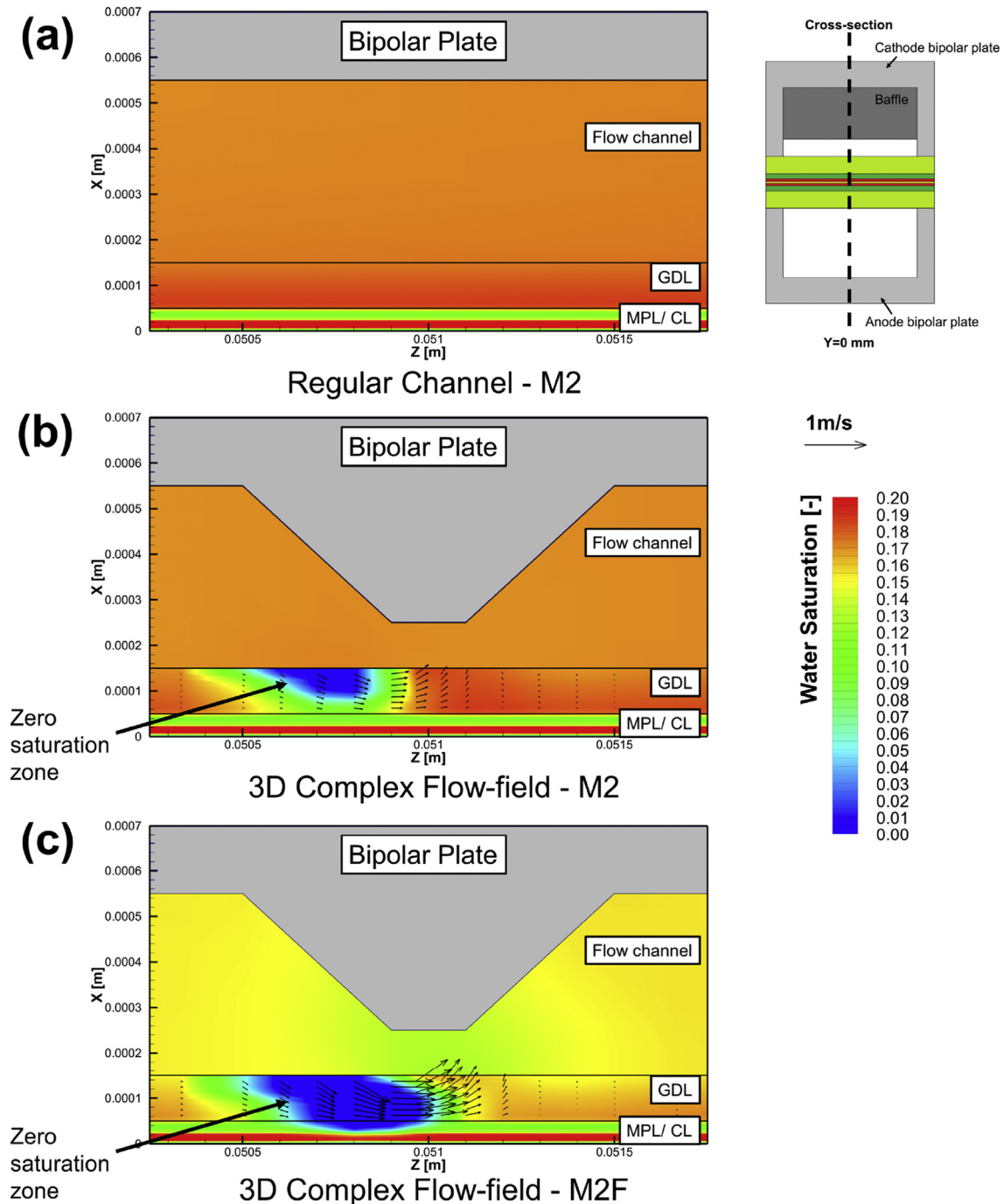

Fig. 5. Contour of water saturation at cathode and gas velocity vector at GDL at mid-channel region ($y = 0$ mm and 50.25 mm $< z < 51.75$ mm) of (a) regular straight channel case (b) 3D complex flow-field case with M^2 simulation (c) 3D complex flow-field case with M^2F simulation.

inertial effect in water removal from GDL since M^2 simulation of 3D complex flow-field shows 15.6% of liquid water removal, while M^{2}F simulation shows roughly twice more liquid water removal.

To elucidate the mechanism of liquid water removal from GDL under Forchheimer's inertial effect in detail, cross-sectional averaged water saturations of GDL at mid-channel region (*48 mm < z<52 mm*) of the three simulation cases are first plotted in Fig. 4. Compared to regular channel case, baseline M^2 simulation of 3D complex flow-field case shows less water at baffle region while showing similar water saturation at non-baffle region. However, M^{2}F model simulation of 3D complex flow-field case shows, overall, less water saturation both at non-baffle region and at baffle region compared to the other two cases. In particular, the liquid water in GDL at baffle region is considerably removed so that the water saturation reaches as low as 5%.

First, the lower water saturation at non-baffle region estimated from M^{2}F model can be explained by enhanced water removal from flow channel due to inertial effect, as discussed in Section 3.1. To illustrate underlying reasons for substantial water removal from GDL under baffle region, water saturation contours of the three simulation cases at a selected cross-section (mid-channel region at *y=0 mm and 50.25 mm < z<51.75 mm*) are shown in Fig. 5 with gas velocity vector fields in GDL. Unlike regular channel case, 3D complex flow-field cases show significant amount of flow penetration from flow channel to GDL under the baffle. It is noteworthy that only gas inside flow channel penetrates to GDL while liquid water is prohibited from flowing into GDL region, as is seen from zero saturation zone in GDL at baffle upstream region. This is mainly due to hydrophobicity of GDL that blocks liquid water flow from channel into GDL by negative capillary pressure. The gas flow penetrates into GDL then further pushes the liquid water and purge out liquid water from GDL to flow channel. In summary, water removal inside GDL under baffle of 3D complex flow-field is attributed to the combined effects of interfacial mass flux at channel/GDL interface and hydrophobicity of GDL.

Specifically, higher gas velocity (as high as 1 m/s) and correspondingly more effective liquid water removal from GDL under baffle are observed under Forchheimer's inertial effect from the comparison of baseline M^2 model and M^{2}F model simulation of 3D complex channel cases. To explain the increase of flow penetration into GDL under inertial effect, interfacial mass flux between flow channel and GDL of the three simulation cases at mid-channel region (*50 mm < z<52 mm*) is plotted with pressure field in Fig. 6. Note that pressures at *z=50 mm* are selected as a reference pressure to compare pressure drop across the selected baffle. It is found that pressure drop across the baffle in 3D complex flow-field case with M^{2}F model simulation is significantly steeper than the other two cases due to inertial loss. Considering that flow in GDL is governed by Darcy's law that gas velocity in GDL is proportional to pressure gradient, more flow penetrates from flow channel into GDL under Forchheimer's inertial effect that removes liquid water from GDL more effectively.

In summary, two main mechanisms of liquid water removal from GDL of PEMFCs with 3D complex flow-field under Forchheimer's inertial effect are found: i) increased liquid water removal from flow channel under Forchheimer's inertial effect, and ii) additional interfacial mass transport between flow channel/GDL due to inertial pressure loss. According to the two mechanisms, liquid water management in GDL can be enhanced by optimizing Forchheimer's inertial effect inside 3D complex flow-field.

3.3. Oxygen transport to CL of PEM fuel cell with 3D complex flow-field

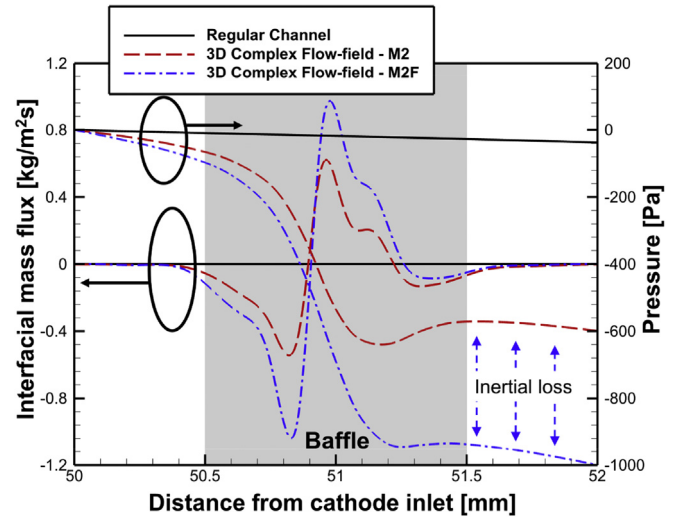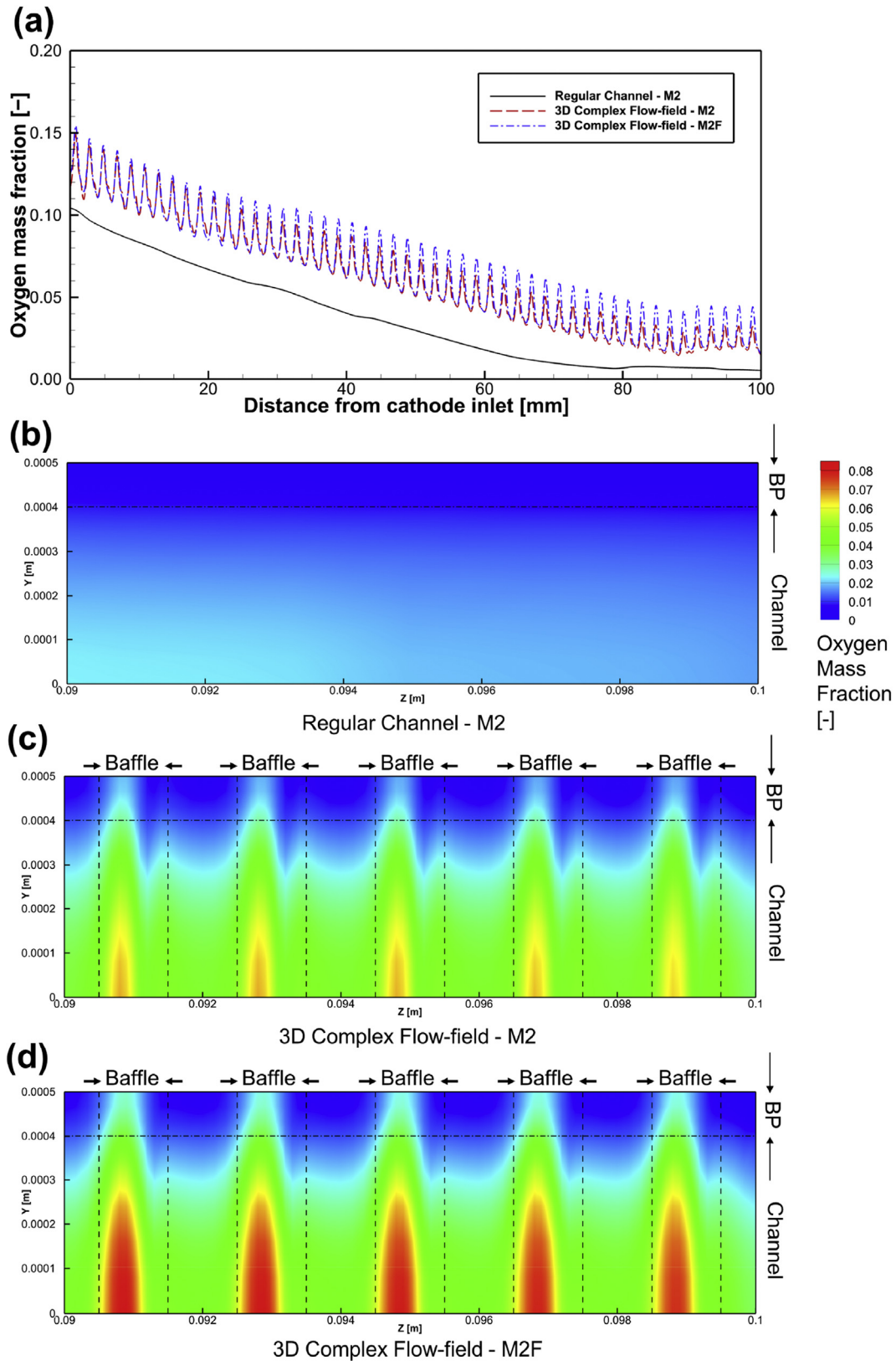Fig. 7 shows oxygen mass fraction profile in CL of three

Fig. 6. Interfacial mass flux and pressure profile at mid-channel region (*50 mm < z < 52 mm*) along flow channel. Pressures at *z = 50 mm* are selected as reference pressures.

simulation cases. Cross-sectional averaged oxygen mass fraction profile in CL is first shown in Fig. 7a to observe overall oxygen distribution along channel direction. Severe oxygen starvation (mass fraction of oxygen < 0.01) at downstream region (*90 mm < z < 100 mm*) is estimated in PEMFCs with regular straight channel, while significantly higher oxygen concentration in CL is estimated at downstream region in PEMFCs with 3D complex flow-fields. To understand the oxygen transport mechanism in depth, contours of oxygen mass fraction at CL/MPL interface at downstream region (*90 mm < z < 100 mm*) are shown in Fig. 7b–d. Compared to regular straight channel case in Fig. 7b and 3D complex flow-field cases show considerably higher oxygen concentration under the baffles. The oxygen mass fraction under baffles is further increased and reaches as high as 0.08 considering Forchheimer's inertial effect in Fig. 7d, compared to the baseline M^2 simulation in Fig. 7c. This can be explained by enhanced interfacial mass transport between flow channel and GDL and liquid water removal due to additional Forchheimer's inertial loss as discussed earlier. However, significant oxygen starvation is still observed at non-baffle region under bipolar plate. This can be alleviated by optimizing 3D flow-field structures. For example, it is possible to use staggered configurations of baffles, rather than in-line configurations of baffles used in this work, in order to supply oxygen and remove liquid water under bipolar plate more effectively by letting gas flow under bipolar plate. Similarly, Heidary et al. [13] numerically showed overall higher oxygen concentration and cell performance by using staggered configurations of blockages than in-line configurations of blockages in flow channel. Optimization of 3D flow-field structures for maximum cell performance using the developed two-phase model is of interest in future work.

3.4. Cell performance of PEMFC with 3D complex flow-field vs. with regular straight flow channel

Cost and durability are the two major concerns for commercialization of PEM fuel cell vehicles. Especially, reducing fuel cell system cost less than $40/kW (2020 U.S. Department of Energy (DOE) target) is essential for future fuel cell system of FCVs, in order to compete with internal combustion engines whose cost is around $25–35/kW [55]. In this section, a comparison of cell performance between PEMFCs with 3D complex flow-fields and regular channels is performed by using the newly developed model to address

Fig. 7. (a) Cross-sectional averaged oxygen mass fraction profile in CL along channel direction, Oxygen mass fraction contour at cathode MPL/CL interface at *90 mm < z < 100 mm* inside (b) regular channel case (c) 3D complex flow-field case with M^2 simulation (d) 3D complex flow-field case with M^2F simulation.

advantages of using 3D complex flow-fields, compared to regular channels. Fig. 8 compares polarization curves of PEMFCs with 3D complex flow-field and regular straight channels. It can be seen

that the cell performance of the PEMFC with regular straight channels is dominated by concentration loss under high current density operation (>3 A cm^{-2}). This implies that long-term
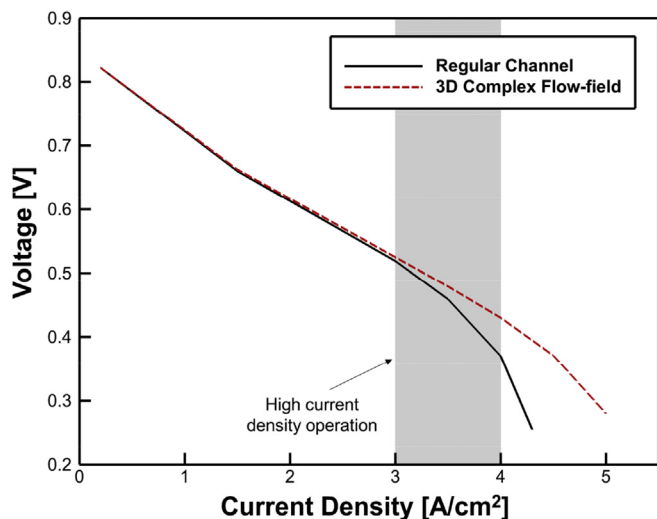
Fig. 8. Polarization curves of PEMFC with regular straight channel and 3D complex flow-field.

operation of PEMFCs with regular straight channels at high current density (>3 A cm^{-2}) is not possible, even using a very thin GDL (100 μm is used in this work), considering that operating a cell under severe oxygen starvation may lead to detrimental cell operational instability and degradation. At this point, one may think of using thinner and more advanced membranes in order to achieve required cell performance for future FCVs, by reducing ohmic loss. However, the membrane used in this study is already quite thin (10 μm) and further reducing it may have consequences of severe membrane failure and degradation.

By using 3D complex flow-fields, one can achieve improvement in both cell performance and durability. As it can be clearly seen in Fig. 8, the PEMFC with 3D complex flow-fields shows linear polarization curve up to 4.3 A cm^{-2}, which is significantly higher than 3.0 A cm^{-2} of the PEMFC with regular straight channels. This is attributed to the Forchheimer's inertial effect in 3D complex flow-fields that substantially enhances mass transport and liquid water removal. As a consequence, one could expect not only improved cell operational stability due to less oxidant starvation and water flooding [56] but also increased cell performance (1.72 W cm^{-2}) at 4 A cm^{-2} compared to the PEMFC with regular straight channels (1.48 W cm^{-2}). This shows that using 3D complex flow-fields is essential for next-generation FCVs, in order to enhance cell operational stability and reduce stack cost per kW. Note that the 3D complex flow-field selected in this study is only a simplified version of complex flow-field in order to study the role of Forchheimer's inertial effect on liquid water removal and mass transport. Therefore, there is still a lot of room for further improvement of high current density cell performance and operational stability, which can be achieved by optimizing of 3D flow-field structures using the present model to minimize the region that suffers from oxygen starvation and liquid water flooding.

4. Conclusions

The recently commercialized fuel cell vehicle "Toyota Mirai" suggests that the next-generation PEMFC systems are likely to feature 3D complex flow-field architecture for enhancing mass transport and liquid water removal at high current density operation, in order to improve cell operation stability and reduce cell manufacture cost per kW. In such complex flow-fields, it is shown that Forchheimer's inertial effect is important, especially under the high current density operation. Therefore, a two-phase model of

PEMFCs with consideration of Forchheimer's inertial effect is proposed for the first time in this work to understand liquid water and mass transport behavior inside PEMFCs with 3D complex flow-field. First, two main mechanisms underlying liquid water removal of PEMFCs with 3D complex flow-field under Forchheimer's inertial effect are revealed: i) enhanced liquid water removal from flow channels that subsequently improves liquid water removal from GDL, and ii) increased micro-scale interfacial mass flux of gas between flow channel and GDL due to additional inertial flow resistance that purge liquid water from GDL more effectively. Second, it is found that oxygen concentration in CL is significantly enhanced by convection caused by baffles in 3D complex flow-field, which is further amplified under Forchheimer's inertial effect. Third, it is anticipated from the proposed model that PEMFCs with 3D complex flow-field are not only more robust, but also produce more power under high current density operation compared to PEMFCs with regular straight flow-fields. As a result, it is shown that high-power and long-term operation of fuel cell system required for next-generation FCVs is possible for PEMFCs with 3D complex flow-fields.

With further progress in increasing catalyst activity and lowering ohmic voltage losses, future PEMFC stacks are expected to operate at current densities higher than 4 A cm^{-2}, which in turn demand for more complex flow-field designs in order to efficiently remove a large amount of product water and hence minimize the mass transport voltage loss. We believe that the proposed macroscopic fuel cell model will serve as a helpful tool for optimization of such sophisticated flow-fields for mass market penetration of FCVs.

References

[1] Y. Tabuchi, T. Shiomi, O. Aoki, N. Kubo, K. Shinohara, Effects of heat and water transport on the performance of polymer electrolyte membrane fuel cell under high current density operation, Electrochim. Acta 56 (2010) 352–360, http://dx.doi.org/10.1016/j.electacta.2010.08.070.

[2] N. Konno, S. Mizuno, H. Nakaji, Y. Ishikawa, Development of compact and high-performance fuel cell stack, SAE Int. J. Altern. Powertrains 4 (2015) 123–129, http://dx.doi.org/10.4271/2015-01-1175.

[3] T. Yoshida, K. Kojima, Toyota MIRAI fuel cell vehicle and progress toward a future hydrogen society, Electochemical Soc. Interface 24 (2015) 45–49.

[4] Y. Nonobe, Development of the Fuel Cell Vehicle Mirai, 2017, pp. 5–9, http://dx.doi.org/10.1002/tee.22328.

[5] H. Heidary, M.J. Kermani, S.G. Advani, A.K. Prasad, Experimental investigation of in-line and staggered blockages in parallel flowfield channels of PEM fuel cells, Int. J. Hydrogen Energy 41 (2016) 6885–6893, http://dx.doi.org/10.1016/j.ijhydene.2016.03.028.

[6] V. Thitakamol, A. Therdthianwong, S. Therdthianwong, Mid-baffle interdigitated flow fields for proton exchange membrane fuel cells, Int. J. Hydrogen Energy 36 (2010) 3614–3622, http://dx.doi.org/10.1016/j.ijhydene.2010.12.060.

[7] S. Han, N. Choi, Y. Choi, Simulation and experimental analysis on the performance of PEM fuel cell by the wave-like surface design at the cathode channel, Int. J. Hydrogen Energy 39 (2014) 2628–2638, http://dx.doi.org/10.1016/j.ijhydene.2013.08.063.

[8] H. Heidary, M.J. Kermani, B. Dabir, Influences of bipolar plate channel blockages on PEM fuel cell performances, Energy Convers. Manag. 124 (2016) 51–60, http://dx.doi.org/10.1016/j.enconman.2016.06.043.

[9] H. Wu, H. Ku, The optimal parameters estimation for rectangular cylinders installed transversely in the flow channel of PEMFC from a three-dimensional PEMFC model and the Taguchi method, Appl. Energy 88 (2011) 4879–4890, http://dx.doi.org/10.1016/j.apenergy.2011.06.034.

[10] A. Ghanbarian, M.J. Kermani, Enhancement of PEM fuel cell performance by flow channel indentation, Energy Convers. Manag. 110 (2016) 356–366, http://dx.doi.org/10.1016/j.enconman.2015.12.036.

[11] M. Dehsara, M.J. Kermani, Proton Exchange Membrane Fuel Cells Performance Enhancement Using, vol. 28, 2014, pp. 365–376, http://dx.doi.org/10.1007/s12206-013-0983-0.

[12] S. Perng, H. Wu, Non-isothermal transport phenomenon and cell performance of a cathodic PEM fuel cell with a baffle plate in a tapered channel, Appl. Energy 88 (2011) 52–67, http://dx.doi.org/10.1016/j.apenergy.2010.07.006.

[13] H. Heidary, M.J. Kermani, A.K. Prasad, S.G. Advani, B. Dabir, Numerical modelling of in-line and staggered blockages in parallel flowfield channels of PEM fuel cells, Int. J. Hydrogen Energy (2016) 1–13, http://dx.doi.org/10.1016/j.ijhydene.2016.10.076.

[14] S. Perng, H. Wu, A three-dimensional numerical investigation of trapezoid

baffles effect on non-isothermal reactant transport and cell net power in a PEMFC, Appl. Energy 143 (2015) 81—95, http://dx.doi.org/10.1016/j.apenergy.2014.12.059.

[15] B. Carnes, D. Spernjak, G. Luo, L. Hao, K.S. Chen, C.Y. Wang, R. Mukundan, R.L. Borup, Validation of a two-phase multidimensional polymer electrolyte membrane fuel cell computational model using current distribution measurements, J. Power Sources 236 (2013) 126—137, http://dx.doi.org/10.1016/j.jpowsour.2013.02.039.

[16] L. Hao, K. Moriyama, W. Gu, C.Y. Wang, Three Dimensional Computations and Experimental Comparisons for a Large-scale Proton Exchange Membrane Fuel Cell, vol. 163, 2016, pp. 744—751, http://dx.doi.org/10.1149/2.1461607jes.

[17] L. Hao, K. Moriyama, W. Gu, C.Y. Wang, Modeling and Experimental Validation of Pt Loading and Electrode Composition Effects in PEM Fuel Cells, vol. 162, 2015, pp. 25—27, http://dx.doi.org/10.1149/2.0221508jes.

[18] T. Kotaka, Y. Tabuchi, U. Pasaogullari, C.Y. Wang, Electrochimica acta impact of interfacial water transport in PEMFCs on cell performance, Electrochim. Acta 146 (2014) 618—629, http://dx.doi.org/10.1016/j.electacta.2014.08.148.

[19] Y. Wang, S. Basu, C.Y. Wang, Modeling Two-phase Flow in PEM Fuel Cell Channels, vol. 179, 2008, pp. 603—617, http://dx.doi.org/10.1016/j.jpowsour.2008.01.047.

[20] T. Henning, J.J. Brandner, K. Schubert, High-speed imaging of flow in micro-channel array water evaporators, Microfluid. Nanofluidics 1 (2005) 128—136, http://dx.doi.org/10.1007/s10404-004-0020-9.

[21] U. Imke, Porous media simplified simulation of single- and two-phase flow heat transfer in micro-channel heat exchangers, Chem. Eng. J. 101 (2004) 295—302, http://dx.doi.org/10.1016/j.cej.2003.10.012.

[22] A.K. Stubos, C. Satik, Y.C. Yortsos, Effects of capillary heterogeneity on vapor liquid counterflow in porous-media, Int. J. Heat. Mass Transf. 36 (1993) 967—976.

[23] D. Sugumar, K.-K. Tio, Thermal analysis of inclined micro heat pipes, J. Heat. Transf. 128 (2006) 198, http://dx.doi.org/10.1115/1.2137763.

[24] K.-K. Tio, C.Y. Liu, K.C. Toh, Thermal analysis of micro heat pipes using a porous-medium model, Heat. Mass Transf. 36 (2000) 21—28, http://dx.doi.org/10.1007/s002310050359.

[25] C.Y. Wang, M. Groll, S. Rösler, C.J. Tu, Porous medium model for two-phase flow in mini channels with applications to micro heat pipes, Heat. Recover. Syst. CHP 14 (1994) 377—389, http://dx.doi.org/10.1016/0890-4332(94)90041-8.

[26] Y. Li, S.-C. Yao, Porous media modeling of microchannel cooled electronic chips with nonuniform heating, J. Thermophys. Heat. Transf. 29 (2015) 695—704, http://dx.doi.org/10.2514/1.T4509.

[27] J.J. Liu, H. Zhang, S.C. Yao, Y. Li, Porous media modeling of two-phase microchannel cooling of electronic chips with nonuniform power distribution, J. Electron. Packag 136 (2014) 21008, http://dx.doi.org/10.1115/1.4027420.

[28] S. Basu, J. Li, C.Y. Wang, Two-phase flow and maldistribution in gas channels of a polymer electrolyte fuel cell, J. Power Sources 187 (2009) 431—443, http://dx.doi.org/10.1016/j.jpowsour.2008.11.039.

[29] F. Jiang, C.Y. Wang, Numerical modeling of liquid water motion in a polymer electrolyte fuel cell, Int. J. Hydrogen Energy 39 (2014) 942—950, http://dx.doi.org/10.1016/j.ijhydene.2013.10.113.

[30] X.G. Yang, Q. Ye, P. Cheng, Matching of water and temperature fields in proton exchange membrane fuel cells with non-uniform distributions, Int. J. Hydrogen Energy 36 (2011) 12524—12537, https://doi.org/10.1016/j.ijhydene.2011.07.014.

[31] J. Kozeny, Ueber kapillare Leitung des Wassers im Boden, Sitzungsber Akad. Wiss 136 (1927) 271—306.

[32] P.C. Carman, Fluid flow through granular beds, Trans. Inst. Chem. Eng. 15 (1937) 150—166.

[33] S. Ergun, A. Orning, Fluid flow through randomly packed columns and fluid-ized beds, Ind. Eng. Chem. 41 (1949) 1179—1184.

[34] J.S. Andrade Jr., U.M.S. Costa, M.P. Almeida, H.A. Makse, H.E. Stanley, Inertial effects on fluid flow through disordered porous media, Phys. Rev. Lett. 82 (1999) 5249.

[35] E.F. Blick, Porous-media momentum equation for highly accelerated flow, SPE Reserv. Eng. (1988) 2—6.

[36] R.D. Barree, M.W. Conway, Beyond Beta Factors: a Complete Model for Darcy, Forchheimer, and Trans- Forchheimer Flow in Porous Media, 2004, p. 8, http://dx.doi.org/10.2523/89325-MS. Spe - 89325.

[37] R.D. Barree, M.W. Conway, Multiphase non-darcy flow in proppant packs, SPE Prod. Oper. (2009) 257—268, http://dx.doi.org/10.2118/109561-MS.

[38] Z. Zeng, R. Grigg, A criterion for non-darcy flow in porous media, Transp. Porous Media 63 (2006) 57—69, http://dx.doi.org/10.1111/j.1439-0523.2006.01169.x.

[39] S.M. Hassanizadeh, High velocity flow in porous media, Transp. Porous Media 2 (1987) 521—531.

[40] I.S. Hussaini, C.Y. Wang, Visualization and quantification of cathode channel flooding in PEM fuel cells, J. Power Sources 187 (2009) 444—451, http://dx.doi.org/10.1016/j.jpowsour.2008.11.030.

[41] A. Ahmadi, A.A. Abbasian Arani, D. Lasseux, Numerical simulation of two-phase inertial flow in heterogeneous porous media, Transp. Porous Media 84 (2009) 177—200, http://dx.doi.org/10.1007/s11242-009-9491-1.

[42] H.S. Lee, I. Catton, Two-phase Flow in Stratified Porous Media, 1986. http://inis.iaea.org/Search/search.aspx?orig_q=RN:18047249. (Accessed 30 January 2017).

[43] X. Liu, F. Civan, R.D. Evans, Correlation of the non-Darcy flow coefficient, J. Can. Pet. Technol. 34 (1995) 50—54, http://dx.doi.org/10.2118/95-10-05.

[44] R.J. Lipinski, A Model for Boiling and Dryout in Particle Beds, 1982. https://inis.iaea.org/search/search.aspx?orig_q=RN:14732098. (Accessed 5 April 2017).

[45] H. Ma, D.W. Ruth, The microscopic analysis of high forchheimer number flow in porous media, Transp. Porous Media 13 (1993) 139—160, http://dx.doi.org/10.1007/BF00654407.

[46] Y. Wang, C.Y. Wang, Modeling polymer electrolyte fuel cells with large density and velocity changes, J. Electrochem. Soc. 152 (2005) A445, http://dx.doi.org/10.1149/1.1851059.

[47] Y. Wang, C.Y. Wang, A Nonisothermal, Two-phase Model for Polymer Electrolyte Fuel Cells, 2008, pp. 0—7, http://dx.doi.org/10.1149/1.2193403.

[48] C.Y. Wang, C. Beckermann, A two-phase mixture model of liquid-gas flow and heat transfer in capillary porous media-I. Formulation, Int. J. Heat. Mass Transf. 36 (1993) 2747—2758, http://dx.doi.org/10.1016/0017-9310(93)90094-M.

[49] C.Y. Wang, P. Cheng, A multiphase mixture model for multiphase, multi-component transport in capillary porous media - I. Model development, Int. J. Heat. Mass Transf. 39 (1996) 3607—3618, http://dx.doi.org/10.1016/0017-9310(96)00036-1.

[50] Y. Wang, C.Y. Wang, A Nonisothermal, Two-phase Model for Polymer Electrolyte Fuel Cells, 2008, pp. 0—7, http://dx.doi.org/10.1149/1.2193403.

[51] E.I. Zoulias, N. Lymberopoulos, Hydrogen-based Autonomous Power Systems, Springer, London, London, 2008, http://dx.doi.org/10.1007/978-1-84800-247-0.

[52] S.V. Patankar, Numerical Heat Transfer and Fluid Flow, Hemisphere Publishing Corp., New York, 1980.

[53] B.R. Hutchinson, G.D. Raithby, A multigrid method based on the additive correction strategy, Numer. Heat. Transf. 9 (1986) 511—537, http://dx.doi.org/10.1080/10407788608913491.

[54] D. Hayashi, A. Ida, S. Magome, Synchrotron x-ray visualization and simulation for operating fuel cell diffusion layers, SAE Tech. Pap. (2017), http://dx.doi.org/10.4271/2017-01-1188.

[55] US DRIVE Fuel Cell Technical Team Roadmap, 2013. https://energy.gov/eere/vehicles/downloads/us-drive-fuel-cell-technical-team-roadmap. (Accessed 4 May 2017).

[56] J. Wu, X.Z. Yuan, J.J. Martin, H. Wang, J. Zhang, J. Shen, S. Wu, W. Merida, A review of PEM fuel cell durability: degradation mechanisms and mitigation strategies, J. Power Sources 184 (2008) 104—119, http://dx.doi.org/10.1016/j.jpowsour.2008.06.006.

List of symbols

c_p: Specific heat (J kg^{-1} K^{-1})
C^i: Molar concentration of species i (mol m^{-3})
D_h: Hydraulic diameter (m)
$D^{i,eff}$: Effective diffusivity of species i (m^2 s^{-1})
$\vec{j}_l$: Mass flux of liquid phase (kg m^{2}s)
K: Thermal conductivity (W m^{-1} K^{-1})
M: Molecular weight (kg mol^{-1})
mf_l^k: Mass fraction of species k in liquid phase
P: Pressure (Pa)
S: Source term in transport equations
S: Water saturation
T: Temperature (K)
U: Characteristic velocity scale (m s^{-1})
$\vec{u}$: Mixture velocity (m s^{-1})

Greek

γ_c: Correction factor for species convection
γ_T: Correction factor for thermal convection
ε: Porosity
κ: Ionomer proton conductivity (S m^{-1})
μ: Dynamic viscosity (kg m^{-1}s^{-1})
ν: Kinematic viscosity (m^2 s^{-1})
ρ: Density (kg m^{-3})
σ: Electronic conductivity (S m^{-1})
τ: Shear stress (N m^{-2})
Φ: Phase potential (V)

Superscript and subscripts

g: Gas
i: Species
k: Phase
l: Liquid
$'$: Non-Darcy Parameter